Available online at www.sciencedirect.com
ScienceDirect
Journal of Sound and Vibration 311 (2008) 39–55
JOURNAL OF SOUND AND VIBRATION
www.elsevier.com/locate/jsvi

Aerodynamic study of three-dimensional larynx models using finite element methods

Marcelo de Oliveira Rosa[a,*], José Carlos Pereira[b]

[a]Departamento de Engenharia Elétrica, Universidade Federal do Paraná, Centro Politécnico, CP 19011, 81531-990 Curitiba, Paraná, Brazil
[b]Departamento de Engenharia Elétrica, Escola de Engenharia de São Carlos, Universidade de São Paulo, Av. Trabalhador sancarlense, 400, 13566-590 São Carlos, São Paulo, Brazil

Received 25 November 2002; received in revised form 1 August 2007; accepted 20 August 2007
Available online 26 October 2007

Abstract

The airflow velocities and pressures are calculated from a three-dimensional model of the human larynx by using the finite element method. The laryngeal airflow is assumed to be incompressible, isothermal, steady, and created by fixed pressure drops. The influence of different laryngeal profiles (convergent, parallel, and divergent), glottal area, and dimensions of false vocal folds in the airflow are investigated. The results indicate that vertical and horizontal phase differences in the laryngeal tissue movements are influenced by the nonlinear pressure distribution across the glottal channel, and the glottal entrance shape influences the air pressure distribution inside the glottis. Additionally, the false vocal folds increase the glottal duct pressure drop by creating a new constricted channel in the larynx, and alter the airflow vortexes formed after the true vocal folds.

1. Introduction

A complete study of the human larynx vibration pattern depends on how the air flows through the larynx and how the pressure is distributed over the laryngeal mucosal walls [1]. Solving the Navier–Stokes equations [2] is the mathematical way to obtain both the airflow velocity and pressure in structures like the larynx. As these equations do not have analytic forms for generic geometric profiles and boundary conditions, numerical methods [3] have to be employed. However, numerical methods demand huge computational efforts to produce feasible solutions. Another alternative is to simplify the Navier–Stokes equations by dividing the larynx channel into several segments with simpler airflow patterns [4–6]: the airflow equations of each segment can be algebraically manipulated in order to define a final set of equations relating lung pressure and larynx volume velocity, which can be solved at high computational speed.

Although the use of less simplified Navier–Stokes equations (including the calculation of airflow pressure and velocity at several spatial points) increases the solution accuracy, it adds more mathematical complexity in

*Corresponding author. Universidade Federal do Paraná, Centro Politécnico, CP 19011, 81531-990, Curitiba, Paraná, Brazil. Tel.: +55 41 3361 3229.
E-mail address: mo-rosa@uol.com.br (M. de Oliveira Rosa).

0022-460X/$ - see front matter © 2007 Elsevier Ltd. All rights reserved.
doi:10.1016/j.jsv.2007.08.037

order to obtain closed-form equations and also increases the solution time. The need for more airflow information led Guo and Scherer [2] to numerically solve full steady Navier–Stokes equations for several larynx profiles. Their calculations of the air volume velocity and pressure for two-dimensional (2D) larynxes demonstrated how accurate and computationally expensive numeric methods could be. The present study expands Guo and Scherer's idea by numerically solving steady Navier–Stokes equations for different three-dimensional (3D) larynx profiles through the finite element methods.

The common procedure to evaluate the pressure distribution over the laryngeal walls is to slice the larynx channel into several small streamwise channels (whose flow patterns are known) in order to create and solve a simpler aerodynamic equation based on simplified conditions (i.e. simplified Navier–Stokes equations). Ishizaka and Flanagan [4] considered the negative pressure formed over the glottal walls as a consequence of the Bernoulli effect (along with tissue spring forces, this negative pressure is responsible for closing the glottis). They also assumed the existence of aerodynamic losses due to the vena contracta formation at the glottis and due to the airflow kinetic pressure loss formed by the sudden channel expansion at the glottal exit (all these effects are caused by airflow viscosity). Later, Ishizaka [7] defined a glottal resistance equation whose coefficients vary according to the laryngeal profile; that is, different losses should be calculated for different glottal shapes in order to correctly compute the airflow pressure and volume velocities in the larynx during phonation.

Miller et al. [5] assumed that there is a set of equations for each laryngeal profile to be solved in order to determine the pressure distribution applied over the glottal walls. Also, their mathematical model includes the aerodynamic effect caused by an assumed formation of vena contracta in the glottal channel entrance because the glottal area does not match the flow area during phonation. Following Ishizaka [7], they considered different aerodynamic behaviours for each streamwise slice of the larynx channel in order to build final sets of equations relating geometric dimensions, flow properties, lung pressure, and mouth pressure to volume velocity.

Finally, Pelorson et al. [6] considered that the flow separation point is dependent of the larynx shape. They developed a flow equation based on boundary-layer approximation specifically to deal with high-Reynolds number flows because they assume that the vena contracta formed over the glottal walls causes low pressure losses. Their formulation also incorporated impulsive flows that occur when the glottis suddenly opens up after its closed phase. They indicated that their flow equation produces a perceptually better glottal and speech waveforms by incorporating these aerodynamic phenomena into their airflow models.

The previous models that incorporate corrective terms to obtain simplified Navier–Stokes equations normally consider these terms as "energy" losses. Because these models do not incorporate any temperature gradient in their formulation, these terms are strictly not energy losses. In fact, these losses are related to air vortexes formed after the glottal constriction, and their geometric and physical characteristics are estimated by experimental studies [4] or by boundary-layer theory [6].

By numerically solving full Navier–Stokes equations, Guo and Scherer [2] determined the airflow pressure and velocity through a 2D larynx model (they specifically focused on only one true vocal fold). They employed the Galerkin finite element method in penalty formulation and created the flow through their fixed larynx model by setting up the boundary conditions of their aerodynamic problem: a fixed constant volume velocity at the inflow surface, which creates the airflow, and zero pressure at outlet surface. They determined the pressure distribution over the mucosal walls for several larynx profiles where it is possible to verify that negative pressures were formed just after the laryngeal constriction with minimal glottal diameter.

As an extension of Guo and Scherer's work [2], the present work analyses the aerodynamic effects produced by the airflow in complete 3D larynx models. Besides the true vocal folds, these geometric models incorporate the false vocal folds and the laryngeal ventricle, which are anatomical structures not considered in Refs. [2,4,6,7]. The boundary conditions that creates the airflow through the larynx model are pressure drops between the inlet and outlet surface model, which are consistent with those found in two-mass models [4,5], but different from Ref. [2]. Mathematically, the finite element method in mixed formulation [8] is used to numerically solve full Navier–Stokes equations and directly gives the airflow pressure and velocity at several spatial 3D points (or nodes) of the larynx model. Different laryngeal profiles (varying the glottis shape and the gap between the false vocal folds) are numerically simulated and the results are discussed.

2. Mathematical methods

Navier–Stokes equations describe the air flowing through the larynx. In the present work, an incompressible, isothermal, laminar, and steady airflow is considered. Because the air flowing through a small constriction has a jet-like shape, the laryngeal airflow can be considered laminar. Additionally, the airflow steadiness is admitted for small time intervals when the larynx walls form "fixed" profiles. Therefore, the final partial differential equations to be solved are

$$\begin{aligned} \nabla \cdot \boldsymbol{U} &= 0, \\ \rho(\boldsymbol{U} \cdot \nabla)\boldsymbol{U} &= \mu(\nabla^2 \boldsymbol{U}) - \nabla P, \end{aligned} \tag{1}$$

where $\boldsymbol{U}$ and P are the air velocity and pressure, respectively, m ($= 0.000179\,\mathrm{dyn\,s/cm^2}$), and r ($= 0.00123\,\mathrm{g/cm^3}$) are the air viscosity and density, respectively.

The finite element method [8] discretizes these airflow equations at a polygonal element level, in which local sets of nonlinear equations are formed. Because of the net effect resulting from coupling all the unstructured mesh elements, a global set of nonlinear equations is constructed by summing all the local set of nonlinear equations. Then, boundary conditions are applied in order to create the flow through the mesh. The solution to every spatial point (node) of the mesh is calculated by using iterative methods.

The elements are polygons of different sizes and here they are tetrahedrons. Second-order polynomials are used to interpolate the velocity inside the finite elements, because they improve the solution accuracy with a reduced number of spatial nodes. However, first-order polynomials for pressure are considered to interpolate pressure in order to keep the problem well posed [9]. Guo and Scherer [2] used the same approach in their 2D finite element method analysis of the laryngeal airflow.

A pressure drop between the inlet and outlet surfaces of the larynx model is established to start the flow. Mathematically, this implies the specification of Neumann boundary conditions at both surfaces, i.e.:

$$\begin{aligned} \mu\frac{\partial U_n}{\partial n} + P &= P_{cte}, \\ \mu\frac{\partial U_s}{\partial n} &= 0, \end{aligned} \tag{2}$$

where $\boldsymbol{U}_n$ and $\boldsymbol{U}_s$ are, respectively, normal and tangential velocity vectors, and P_{cte} is the inlet or outlet pressure, according to the model boundary surface. It means that the "do-nothing" boundary condition [10] is adopted. Dirichlet boundary conditions are used by setting the velocity to zero over the larynx walls (i.e., the remaining surfaces in the larynx model).

Instead of using the Galerkin finite element method approach to discretize Navier–Stokes equations at the element level [2], a hybrid approach [11] is used to handle inherited difficulties of controlling numerical instabilities [3] related to the convection term—$(\boldsymbol{U} \cdot \bigtriangledown)\boldsymbol{U}$—of Navier–Stokes equations. This hybrid approach blends methods with different accuracy and robustness in order to discretize Navier–Stokes equations according to the velocity gradients along the simulated laryngeal cavity. The first-order method (FOM) [12] and streamline upwinding/Petrov Galerkin (SUPG) [13] confer, respectively, robustness and accuracy to the flow solution. The blending factor g is calculated through the mesh using the technique proposed in Ref. [13], which is based on the local velocity gradient: spatial regions with low gradients are mainly discretized by SUPG while those with high gradients are mainly discretized by first-order method. It is important to mention that all these methods apply certain amounts of artificial diffusion in order to control the numerical wiggles (wiggles are oscillations of the velocity vectors due to the lack of nodes used when computing the flow in high-gradient regions). Mathematically, the hybrid approach can be represented by

$$\mathrm{HYBRID(PDE)} = \gamma\,\mathrm{SUPG(PDE)} + (1-\gamma)\mathrm{FOM(PDE)}, \tag{3}$$

where SUPG(PDE) and FOM(PDE) are discrete operators of streamline upwinding/Petrov Galerkin and first-order methods, respectively, applied over partial differential equations and g γ is the blending factor.

After discretizing the differential partial equations at the element level, the global set of nonlinear equations is formed by summing all local sets of nonlinear equations and is represented by the following matrix

equation:

$$A(\boldsymbol{X})\boldsymbol{X} = \boldsymbol{B}, \tag{4}$$

where A contains the airflow physical behaviour, $\boldsymbol{B}$ contains the boundary conditions (zero velocity at mucosal walls and pressure drop between inlet and outlet larynx surfaces), and $\boldsymbol{X}$ contains the velocities and pressures at all the mesh nodes.

A successive substitution procedure [8] is used to solve Eq. (4), starting from a null solution ($\boldsymbol{X}_0 = 0$), i.e.:

$$\begin{aligned} A(\boldsymbol{X}_{n-1})\boldsymbol{X}_* &= \boldsymbol{B}, \\ \boldsymbol{X}_n &= \alpha\boldsymbol{X}_* + (1-\alpha)\boldsymbol{X}_{n-1}, \end{aligned} \tag{5}$$

where α (the relaxation factor) $= 0.5$, $\boldsymbol{X}_{n-1}$ and $\boldsymbol{X}_n$ are the solution at the previous and current iterative steps ($\boldsymbol{X}_*$ is the solution to be relaxed by the method).

The stop condition for this iterative method [8] is given by

$$\frac{|\boldsymbol{X}_n - \boldsymbol{X}_{n-1}|}{|\boldsymbol{X}_n|} \leqslant 0.001. \tag{6}$$

In order to speed up the solution to Eq. (4), the reduced basis method [14] is employed. This method consists of determining several bases from where a projected—and therefore, estimated solution will be calculated. This estimated solution constitutes the "best guess" to be applied in successive substitution method—Eq. (5)—instead of $\boldsymbol{X}_0 = 0$.

The bases consist of subsolutions for several subproblems generated from the actual problem. The difference between all these subproblems is a scalar parameter (normally the Reynolds number). Here, instead of applying a full pressure drop (ΔP) in order to calculate the final airflow solution, several subproblems are defined from different small pressure drops (ΔP_i) and Eq. (5) is used to solve them. The reduced basis method can be described by the following steps:

1. Calculate first base $\boldsymbol{X}_{0\text{th\_base}}$ with pressure drop equals to ΔP_0 and $\boldsymbol{X}_0 = 0$.
2. Calculate additional bases $\boldsymbol{X}_{1\text{st\_base}},\ldots,\boldsymbol{X}_{4\text{th\_base}}$ with pressure drop equal to $\Delta P_1,\ldots,\Delta P_4$ by solving Eq. (4) and $\boldsymbol{X}_0 = \boldsymbol{X}_{0\text{th\_base}},\ldots,\boldsymbol{X}_{3\text{rd\_base}}$, respectively.
3. Calculate the final approximated solution $\boldsymbol{X}_{\text{reduced\_base}}$ from bases $\boldsymbol{X}_{0\text{th\_base}},\ldots,\boldsymbol{X}_{4\text{th\_base}}$.
4. Calculate the final solution $\boldsymbol{X}_{\text{solved}}$ with the final pressure drop ΔP by solving Eq. (4) and $\boldsymbol{X}_0 = \boldsymbol{X}_{\text{reduced\_base}}$.

In the current problem, 5 bases are employed considering the trade-off between convergence speeds and computational efforts. A specific pressure drop value is set (ΔP_4) and the others are determined as its fractions ($\Delta P_0 = \Delta P_4/5$, $\Delta P_1 = 2\Delta P_4/5$, $\Delta P_2 = 3\Delta P_4/5$, and $\Delta P_3 = 4\Delta P_4/5$).

Of course, the parameter ΔP_4 is dependent on mesh density, Reynolds number, and geometric characteristic of the problem. Therefore, its choice is based on empiric studies carried over several simulations. It is important to mention that high values produce a good estimation for $\boldsymbol{X}_{\text{reduced\_base}}$ and accelerate the final convergence steps. However, the subsolutions for high pressure drops are difficult of obtaining for high Reynolds number flows. On the other hand, the sub-solutions calculated for low pressure drops are easier of obtaining but they produce $\boldsymbol{X}_{\text{reduced\_base}}$ too far from $\boldsymbol{X}_{\text{solved}}$. This means that all difficulties with nonlinear problems are transferred to the final convergence steps. In the current case, ΔP_4 is set to $50\,\text{dyn/cm}^2$. As mentioned, this value is based on empiric studies carried through several laryngeal profiles and further studies should be developed in order to determine a good ΔP_4 for the larynx in pathological conditions, for example.

All the presented strategies (starting from the use of stabilised methods to discretize airflow convection terms, up to the reduced basis method to speed up the solution to nonlinear equation systems) are well documented in the literature and further discussions of their mathematical aspects (convergence and robustness) are beyond the scope of this article. Their use is justified by the presence of high velocity and pressure gradients produced in the airflow passing through the larynx (especially after the glottal constriction), which increases instabilities in the solution to Navier–Stokes equations.

3. The larynx models

The spatial boundaries of the simulated laryngeal channels are described from several ellipses according to Eq. (7). They are obtained by "slicing" the channel across horizontal planes:

$$\begin{aligned} x = R_1\cos(\theta), \quad y = R_1\sin(\theta), \quad 0 \leqslant \theta \leqslant \pi/2, \\ x = R_2\cos(\theta) \quad y = R_2\sin(\theta), \quad \pi/2 \leqslant \theta \leqslant \pi, \\ x = R_3\cos(\theta), \quad y = R_3\sin(\theta), \quad \pi \leqslant \theta \leqslant 3\pi/2, \\ x = R_4\cos(\theta), \quad y = R_4\sin(\theta), \quad 3\pi/2 \leqslant \theta \leqslant 2\pi, \end{aligned} \tag{7}$$

where x and y form a spatial position in the horizontal plane at the defined "ellipse", and R_1, R_2, R_3, and R_4 are the radii of this "ellipse".

Using these formulas, three different laryngeal profiles are constructed. They are presented in Tables 1–3 and constitute the three basic shapes that a normal larynx can assume: parallel, convergent and divergent profiles, as shown in Fig. 1. This picture also introduces the true vocal folds (1), laryngeal ventricle (2), and false vocal folds (3). The inlet and outlet surfaces, where the lung and supraglottal pressures are, respectively, specified, are also presented. Note that Eq. (7) can produce smooth versions of the larynx (considering the

Table 1
Geometric description of a larynx with parallel profile

Section	Center (cm)	Radius R1, R2, R3, and R4 (cm)
S0	0, 0, −2	0.7, 0.7, 0.7, 0.7
S1	0, 0, −1	0.7, 0.7, 0.7, 0.7
S2	0, 0, −0.8	0.7, 0.7, 0.7, 0.7
S3	0, 0, −0.61	0.7, 0.6, 0.7, 0.6
S4	0, 0, −0.47	0.7, 0.25, 0.7, 0.25
S5	0, 0, −0.40	0.7, 0.075, 0.7, 0.075
S6	0, 0, −0.33	0.7, 0.025, 0.7, 0.025
S7	0, 0, −0.26	0.7, 0.025, 0.7, 0.025
S8	0, 0, −0.19	0.7, 0.025, 0.7, 0.025
S9	0, 0, −0.12	0.7, 0.025, 0.7, 0.025
S10	0, 0, −0.05	0.7, 0.025, 0.7, 0.025
S11	0, 0, 0	0.7, 0.235, 0.7, 0.235
S12	0, 0, 0.03	0.7, 0.35, 0.7, 0.35
S13	0, 0, 0.07	0.7, 0.5, 0.7, 0.5
S14	0, 0, 0.10	0.7, 0.515, 0.7, 0.515
S15	0, 0, 0.23	0.7, 0.45, 0.7, 0.45
S16	0, 0, 0.35	0.7, 0.46, 0.7,0.46
S17	0, 0, 0.48	0.7, 0.6 0.7, 0.6
S18	0, 0, 0.60	0.7, 0.7, 0.7, 0.7
S19	0, 0, 1.30	0.7, 0.7, 0.7, 0.7
S20	0, 0, 2	0.7, 0.7, 0.7, 0.7

Table 2
Geometric description of a larynx with convergent profile (the remaining sections are the same as those shown in Table 1)

Section	Center (cm)	Radius R1, R2, R3, and R4 (cm)
S6	0, 0, −0.33	0.7, 0.065, 0.7, 0.065
S7	0, 0, −0.26	0.7, 0.055, 0.7, 0.055
S8	0, 0, −0.19	0.7, 0.045, 0.7, 0.045
S9	0, 0, −0.12	0.7, 0.035, 0.7, 0.035
S10	0, 0, −0.05	0.7, 0.025, 0.7, 0.025
Angle		−8.13°

Table 3
Geometric description of a larynx with divergent profile (the remaining sections are the same as those shown in Table 1)

Section	Center (cm)	Radius R1, R2, R3, and R4 (cm)
S6	0, 0, −0.33	0.7, 0.025, 0.7, 0.025
S7	0, 0, −0.26	0.7, 0.035, 0.7, 0.035
S8	0, 0, −0.19	0.7, 0.045, 0.7, 0.045
S9	0, 0, −0.12	0.7, 0.055, 0.7, 0.055
S10	0, 0, −0.05	0.7, 0.065, 0.7, 0.065
Angle		+8.13°

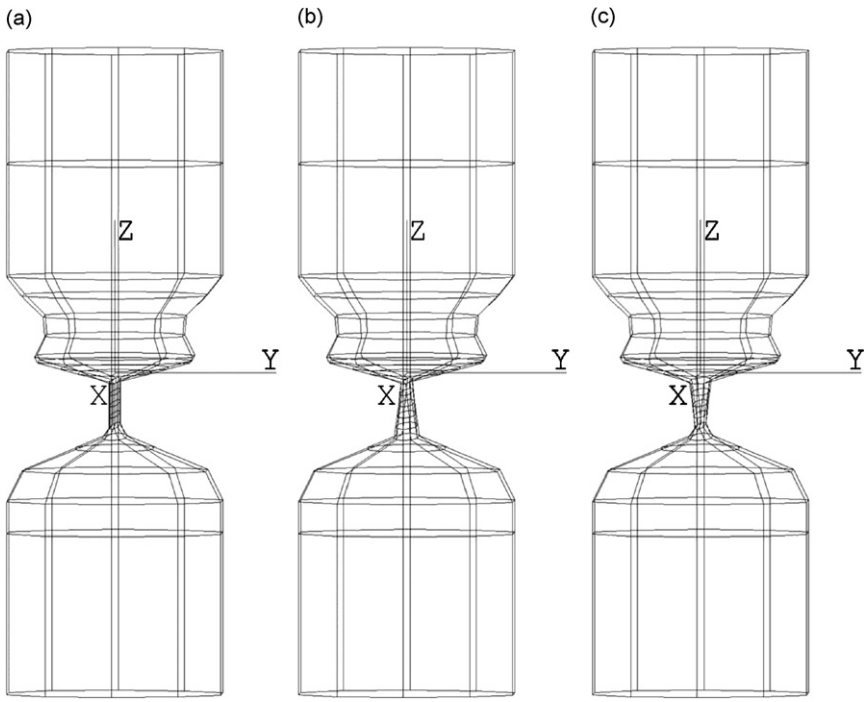

Fig. 1. 3D view of normal larynxes with parallel (a), convergent (b), and divergent (c) profiles. The sections at the bottom and at the top of all three larynx models are S0 and S20, respectively. All the larynxes include true vocal folds, laryngeal ventricle and false vocal folds.

larynx descriptions given by Tables 1–3). All these ellipses are equally divided into 6 segments. By connecting adjacent segments of adjacent ellipses produces surface meshes as shown in Fig. 1.

An automatic mesh algorithm constructs the tetrahedrons by using the surface mesh as reference. The total number of tetrahedrons is 2600, resulting in 4151 airflow nodes and 651 pressure velocity nodes. The nodal distribution through the model is constant, i.e., the number of nodes and tetrahedrons between sections S_i and S_{i+1} is equal to those between sections S_{i+1} and S_{i+2} (these sections are defined in Tables 1–3). It means that the larynx mesh is denser in regions whose sections have smaller areas. Fig. 2 shows an example of larynx meshes used in this work.

4. Results and discussions

To create the flow in the simulated larynxes, the lung pressure was set to 8000 dyn/cm^2 while the ''mouth'' pressure was set to 0 dyn/cm^2, resulting in a pressure drop (ΔP) equal to 8000 dyn/cm^2. The solutions to Navier–Stokes equations for three proposed profiles show that a negative pressure is formed just after the constriction with minimal glottal area—its exactly location demands calculation using finer larynx meshes and

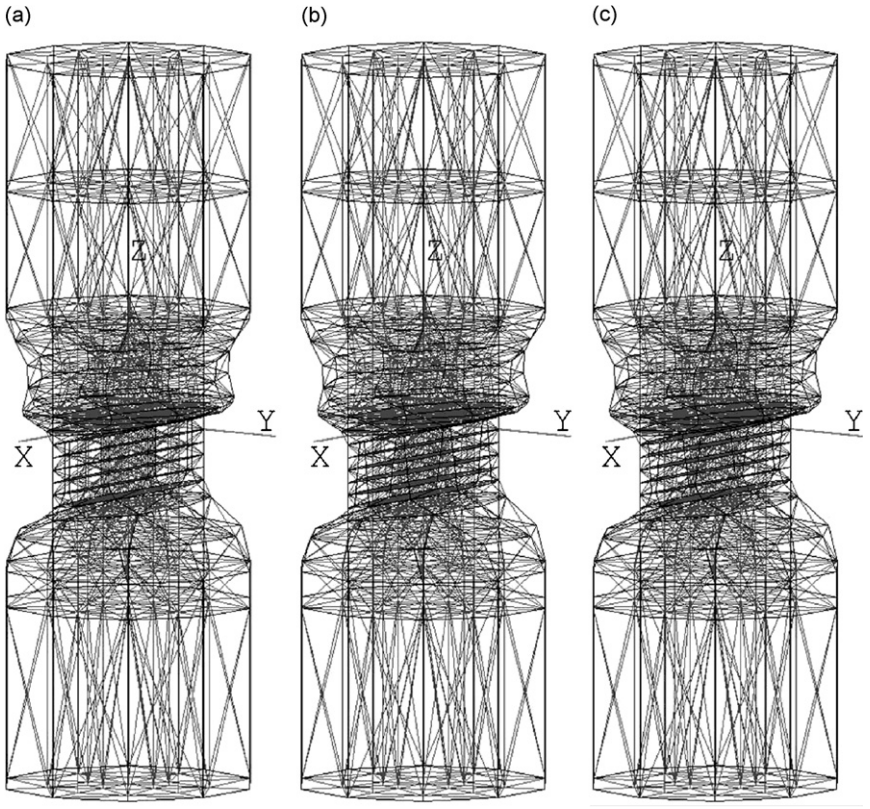

Fig. 2. 3D view of normal larynx meshes with parallel (a), convergent (b), and divergent (c) profiles. All the meshes are defined by tetrahedrons.

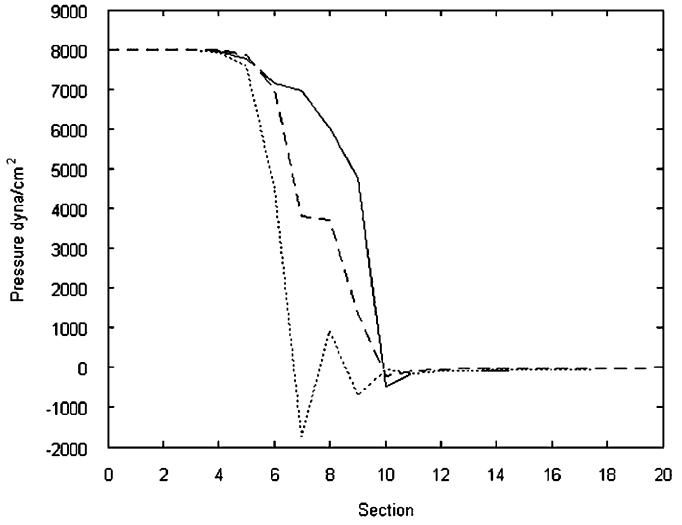

Fig. 3. Mean pressure distribution along the sections of larynxes in convergent (——), divergent (·····) and parallel (––) profiles.

a glottal entrance more rounded. This happens because the modelling assumption of an incompressible flow imposes an airflow re-circulation after this section. Given the 3D aspect of this work, we define "mean pressure" as the average of pressures collected at a single elliptical section. Fig. 3 presents the mean pressure calculated along all the laryngeal elliptical sections.

4.1. Pressure distribution

The parallel profile produced the smoothest glottal duct pressure distributions because the airflow was affected only by viscosity, not by glottal duct area change (as in Ref. [15]). In the other two profiles, the section with minimal area defined the location of the highest pressure gradient.

In the parallel and divergent laryngeal profiles, the air pressure upstream to the constriction with minimal area (before sections S5 in Table 1, and S6 in Table 3) presented numeric value close to the lung pressure. However, the air pressure gradient in the glottal channel was lower for the parallel profile (maximum of 3199.15 dyn/cm^3) than for the divergent (maximum of 6206.73 dyn/cm^3) and convergent ones (maximum of 5223.39 dyn/cm^3).

Considering the aerodynamic forces applied over the glottis, upstream mucosal surfaces (from sections S3 to S5) were under influence of positive pressures (close to lung pressure) while downstream mucosal surfaces (from sections S10 to S13) were under influence of zero or negative pressures. The resulting pressure difference produces an aerodynamic force that should push the glottis upward. The exactly direction of this force vector will be dependent of the curvature of the true vocal folds and the pressure distribution over the glottal walls. A potential effect of this aerodynamic force distribution is that stress and shear forces developed in the larynx tissues are nonlinear even if such tissues are described by linear tissue models.

Scherer et al. [16] indicate that transglottal pressure drop for parallel profiles significantly begins in sections located upstream to the glottal entry (tap 4 in Ref. [16]), which is confirmed by Fig. 3 (section S5). To compare both models, the pressure drop between the pressures gathered at upstream sections (tap 4 in Ref. [16] and section S5) and at the glottal entry (tap 6 in Ref. [16] and section S6) was computed. The ratio between this pressure drop to the pressure gathered at upstream sections indicated a pressure fall of 80% and 12.5% for the model from Ref. [16] and the parallel profile presented here, respectively. Clearly, the glottal entrance shape has significant influence in this difference. Rounded shapes for glottal entrances cause significant pressure drops upstream to the glottal channel while sharp glottal entrances induce air pressures, whose values are close to lung pressure, over mucosal walls located upstream to the glottal channel.

In the divergent profile, a negative pressure appeared downstream to the section with minimal glottal area. In models with smoother glottis entrances [17,18], the minimum pressure occurs exactly over the laryngeal section with the minimal glottal area while here it occurred after the section with minimal glottal area. The ratio of the minimum glottal pressure to the transglottal pressure was −21.23% and −35% for results from Fig. 3 and [18], respectively, which emphasises the effects of different glottal entrance shapes over air pressure distribution.

The main aspect of the pressure distribution in the divergent profile is that the progressive expansion of the channel inside the glottis and the position of the constriction with minimal area located near the entrance of the glottis contribute to the formation of negative pressures inside the glottal channel.

A secondary negative pressure appeared close to the glottis exit (section S10) separated from the minimal (also negative) pressure located near the glottis entrance (section S7) by a positive pressure. In Ref. [18], two negative valleys are clearly presented in pressure profiles for 10 and 15 cm H_2O transglottal pressures, respectively located at tap 6 and tap 11, and the pressure at tap 11 is located near the glottis exit. Although the pressures between taps 6 and 11 are not positive air pressures, they are higher than the pressures gathered at both taps. The ratios of this secondary negative pressure to the transglottal pressure were −7.5% and −6.0% from Fig. 3 and [18], respectively. This pressure behaviour might happen because the larynx has actually two channel expansions: one located inside the glottis and one located downstream the glottis. The shape of the glottis entrance is responsible for the difference between both models in relation to the ''positive'' pressure values located between these two negative pressures. Note that the results of [18] are smoother than those presented here because they used 15,000 and 126,000 nodes to solve Navier–Stokes equations for 2D symmetric and asymmetric larynx profiles.

A comparison of the results for convergent profiles shown in Fig. 3 and [19] revealed that their pressure distributions are very similar. Although the glottal entrance shapes of both models are different, their aerodynamic effect inside the convergent glottis does not produce a significant difference in the position of negative pressures, which are formed near the glottal exit. As [19] indicates, the location of minimum pressure

in the glottis is function of the exit radius: the present 3D model has an exit radius equal to zero, which results in a minimum pressure located exactly over the glottal exit.

To confirm the physical findings shown in Fig. 3, the glottal area of all three laryngeal profiles was increased. Tables 4–6 describe these larynxes and Fig. 4 shows the mean pressure distribution through the transverse sections. In order to quantify the effects of this glottal area change, the pressure difference between sections S5 and S10 in Table 1–3 was calculated. The change of +80% in the minimal glottal channel area (from 0.05143 to 0.09258 cm^2) produced a change of −11.985%, −4.212%, and −1.283% in that pressure difference for the divergent, parallel and convergent larynxes, respectively.

This change in the minimal glottal channel area also altered the minimum pressure from −213.35 to −485.81 dyn/cm^2 for the parallel profile, from −458.48 to −657.48 dyn/cm^2 for the convergent profile, and −1725.00 to −1800.56 dyn/cm^2 for the divergent profile. This is a consequence of the increase in volume velocity that demands lower negative pressures to numerically sustain the incompressibility of the laryngeal air. Fig. 4 confirms that divergent profiles produce the lowest negative pressure among the laryngeal profiles, independent of the glottal aperture.

Table 4
Geometric description of a larynx with enlarged glottis and parallel profile (the remaining sections are the same as those shown in Table 1)

Section	Center (cm)	Radius R1, R2, R3, and R4 (cm)
S6	0, 0, −0.33	0.7, 0.045, 0.7, 0.045
S7	0, 0, −0.26	0.7, 0.045, 0.7, 0.045
S8	0, 0, −0.19	0.7, 0.045, 0.7, 0.045
S9	0, 0, −0.12	0.7, 0.045, 0.7, 0.045
S10	0, 0, −0.05	0.7, 0.045, 0.7, 0.045
Angle		0°

Table 5
Geometric description of a larynx with enlarged glottis and convergent profile (the remaining sections are the same as those shown in Table 1)

Section	Center (cm)	Radius R1, R2, R3, and R4 (cm)
S5	0, 0, −0.33	0.7, 0.095, 0.7, 0.095
S6	0, 0, −0.33	0.7, 0.085, 0.7, 0.085
S7	0, 0, −0.26	0.7, 0.075, 0.7, 0.075
S8	0, 0, −0.19	0.7, 0.065, 0.7, 0.065
S9	0, 0, −0.12	0.7, 0.055, 0.7, 0.055
S10	0, 0, −0.05	0.7, 0.045, 0.7, 0.045
Angle		−8.13°

Table 6
Geometric description of a larynx with enlarged glottis and divergent profile (the remaining sections are the same as those shown in Table 1)

Section	Center (cm)	Radius R1, R2, R3, and R4 (cm)
S6	0, 0, −0.33	0.7, 0.045, 0.7, 0.045
S7	0, 0, −0.26	0.7, 0.055, 0.7, 0.055
S8	0, 0, −0.19	0.7, 0.065, 0.7, 0.065
S9	0, 0, −0.12	0.7, 0.075, 0.7, 0.075
S10	0, 0, −0.05	0.7, 0.085, 0.7, 0.085
Angle		+8.13°

4.2. Pressure distribution within laryngeal sections

Figs. 5–7 allow a detailed examination of the pressure gradient in particular sections of parallel, convergent and divergent profiles, respectively.

In sections located in the vicinity of minimal glottal area, the pressure in the laryngeal commissures was higher than the pressure formed at the medial region of the glottis. Therefore, the airflow was forced to concentrate and assume a jet-like shape. Figs. 5 (S6, S7, and S9), 6 (S9) and 7 (S6 and S7) show this phenomenon.

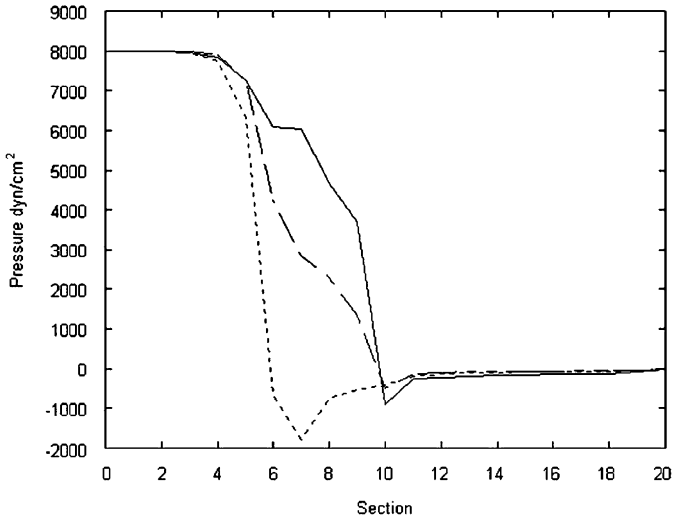

Fig. 4. Mean pressure distribution along the sections of larynxes in convergent (——), divergent (⋯⋯) and parallel (– –) profiles with an enlarged glottis.

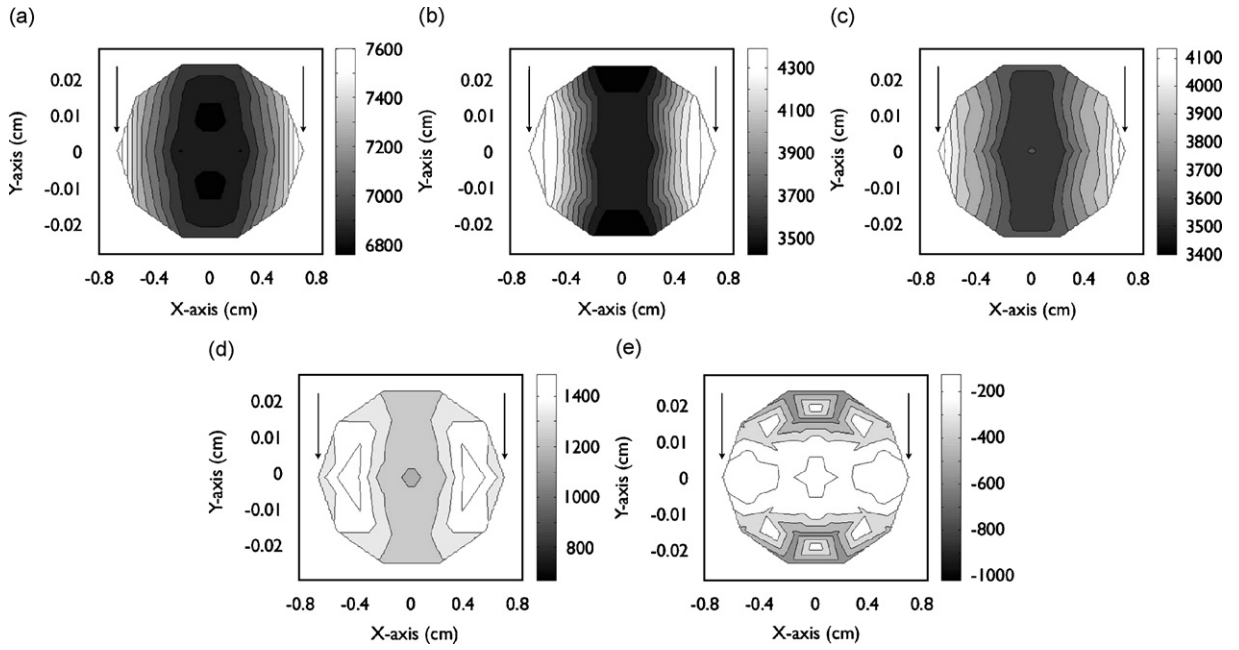

Fig. 5. Pressure distribution (in dyn/cm^2) over the surface of sections S6 (a), S7 (b), S8 (c), S9 (d), and S10 (e) of a larynx with a parallel profile. Arrows point at the anterior and posterior commissures.

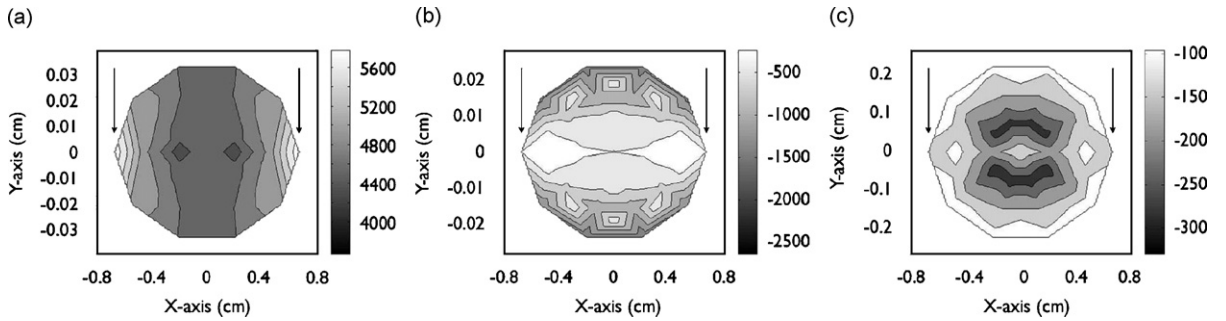

Fig. 6. Pressure distribution (in dyn/cm^2) over the surface of sections S9 (a), S10 (b), and S11 (c) of a larynx with a convergent profile. S10 (b) is the minimal area section. Arrows point at the anterior and posterior commissures.

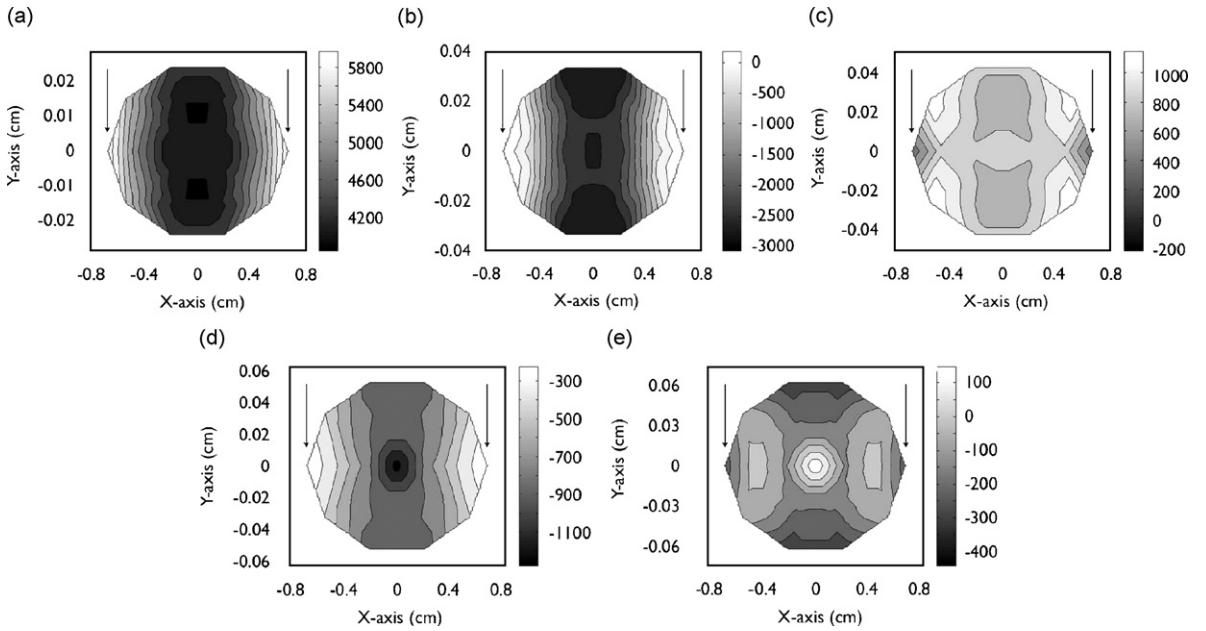

Fig. 7. Pressure distribution (in dyn/cm^2) over the surface of sections S6 (a), S7 (b), S8 (c), S9 (d), and S10 (e) of a larynx with a divergent profile. S6 (a) is the minimal area section. Arrows point at the anterior and posterior commissures.

Section 10, represented in Fig. 5, shows that in the parallel profile negative pressures were formed over the mucosal walls in the medial region of the glottis, while positive pressures occurred over commissures walls. Also, pressures inside this section were lower than pressures in its boundaries. Scherer and Alipour [15] indicate the same result for their hemilarynx experiments. In Fig. 5, an analysis of the pressures gathered from the medial region of the glottis revealed the same finding, which is more evident in section S10.

In the convergent profile, the abrupt change in pressure (from positive to negative values) occurred in the vicinity of section S10. Its pressure distribution (S10 in Fig. 6) was similar to that presented by section S10 in Fig. 5 (parallel profile). In section S11, the more negative pressures formed in the medial region of the glottal section indicated that the airflow kept its convergent shape, despite the sudden expansion after the glottal channel. However, the longitudinal pressure gradient was lower than the intra-section one, which means that the convergent shape had a tendency to spread out the airflow in the anterior–posterior direction.

The negative pressures were formed in section S7 of the divergent profile (Fig. 7), specifically at mucosal surfaces of the glottis medial region while the commissure surfaces had positive pressures. Section S8 in Fig. 7

presents a positive pressure and surface points near the laryngeal commissures had lower pressure values (Fig. 4).

Other negative pressures were also formed in section S9. Basically, the pressure distribution in this section is similar to that produced in section S7. Negative pressures were also found in section S10 where a divergent opening was formed, but their magnitudes were lower than those found in previous sections.

Analysing the pressure gradient within all the laryngeal sections, the divergent laryngeal profile produced the highest pressure gradient (3583.37 dyn/cm^3 in section S8), followed by convergent profile (2668.23 dyn/cm^3 in section S11) and parallel profile (1064.70 dyn/cm^3 in section S8). High pressure gradients in these sections and in the vicinity of these sections tend to funnel the airflow velocity vectors for all the simulated larynxes as described next.

4.3. Airflow analysis

In all the larynxes of this study, regions in the larynx channel with high pressure gradient generated airflow velocities with higher magnitudes. Therefore, this phenomenon—induced by keeping the volumetric velocity constant along the larynx channel—specifically happened inside the glottal channel. According to Table 7, the highest airflow velocities were located at section S7 for convergent profile and section S10 for both parallel and divergent profiles. It means that these airflow velocities are located inside the glottis near the larynx section with the minimal area.

Additionally, Fig. 8 shows that the flow was not parallel to the mucosal walls in the longitudinal view. The anterior and posterior commissures tended to funnel the airflow in a convergent shape through the glottis in the last picture of Fig. 8. Of course, the convergent nature of the flow near the commissure region indicated that portions of the re-circulation zone naturally formed over the laryngeal ventricle and the false vocal folds

Table 7
Location, value and magnitude of the highest air flow velocities for larynxes with parallel, convergent and divergent profiles

Profile	Location (cm)	Vector velocity (cm/s)	Magnitude of the vector velocity (cm/s)
Parallel	0, 0, −0.26	−3.70, 0, 2426.75	2426.75
Convergent	0, 0, −0.05	13.32, 17.98, 2824.41	2824.49
Divergent	0, 0, −0.26	−19.42, −0.03, 3776.55	3776.6

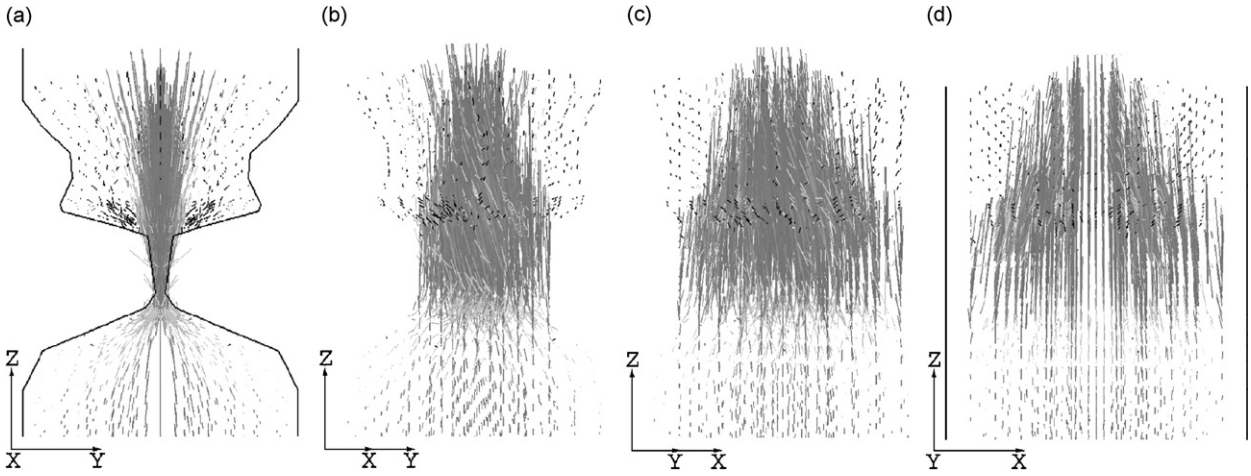

Fig. 8. 3D airflow velocity vectors in a larynx with divergent profile from different viewpoints: coronal plane (a), 30° from coronal plane (b), 60° from coronal plane (c), and saggital plane (d). Lighter vectors point downstream and darker vectors point upstream.

(as shown in the second and third pictures of Fig. 8) start near the anterior and posterior commissures. 2D and simplified models should consider this vortex formation when they estimate the aerodynamic losses in their models.

Additionally, the airflow velocities resulted from the divergent profile (Fig. 8) shown some velocity vectors inside the glottis point toward the vocal fold tissue instead of upward. It indicates that the presence of a positive pressure region followed by a secondary negative pressure region influences the glottal airflow. Considering results showing velocity vectors from Refs. [2,17,18], the vortex formed after the glottal channel actually started within the glottis. To confirm this, a denser mesh should be considered in order to obtain more detailed velocity vectors from laryngeal airflow simulations.

4.4. The influence of false vocal folds

The false vocal folds alter the laryngeal airflow. To support this statement, larynxes for parallel, convergent, and divergent profiles (Tables 1–3) had some of their sections altered to capture three different false vocal fold gaps. Table 8 shows these geometric changes (the geometry of true vocal folds is kept constant). These gaps were near the average values found for phonating humans (0.613 and 0.439 cm for non-singer male and female, respectively), and the largest gap was within 2 standard deviations for males [20].

Figs. 9 and 10 present the difference between the mean pressure distribution curves for larynxes with and without the false vocal folds (for pressure distribution in a larynx with true vocal folds in divergent profile, see [21]). The shape of these folds was divergent.

The presence of false vocal folds negligibly influenced the airflow pressure distribution in the larynx, although the magnitude of negative pressures was increased when the section areas of the false vocal channel are decreased, a relationship that happened for all the three glottal profiles. This phenomenon can be attributed to the fact that false vocal folds acted as an extension of the glottal channel to the airflow and reduced the vortex size formed in the supra-glottal channel as shown in Fig. 11 for a larynx with divergent glottis.

As stated in Ref. [17], the false vocal folds in larynx models guide the airflow and avoid the skewing of the airflow in symmetric profiles. In Figs. 8 and 11, the airflow was fully symmetric along the simulated profiles. It is important to consider that numerical methods using artificial diffusion in order to stabilise the convection terms of Navier–Stokes equations tend to remove the skewing of airflow in simulated symmetric channels [8,11].

For convergent and parallel larynx profiles with different false vocal fold sizes, the mean pressure distribution curves had different behaviours in sections located downstream of that with minimal glottal area. Specifically, there was an increase in the mean pressure for some curves instead of a decrease. The flow pattern

Table 8
Geometric description of three false vocal folds with divergent profile (the remaining sections for normal larynxes are the same as those shown in Tables 1–3)

Type of FVF	Section	Center (cm)	Radius R1, R2, R3, and R4 (cm)
Without FVF	S15	0, 0, 0.23	0.7, 0.7, 0.7, 0.7
	S16	0, 0, 0.35	0.7, 0.7, 0.7, 0.7
	Angle		0°
Widest FVF gap	S15	0, 0, 0.23	0.7, 0.45, 0.7, 0.45
	S16	0, 0, 0.35	0.7, 0.46, 0.7, 0.46
	Angle		+4.76°
Medium FVF gap	S15	0, 0, 0.23	0.7, 0.35, 0.7, 0.35
	S16	0, 0, 0.35	0.7, 0.36, 0.7, 0.36
	Angle		+4.76°
Narrowest FVF gap	S15	0, 0, 0.23	0.7, 0.25, 0.7, 0.25
	S16	0, 0, 0.35	0.7, 0.26, 0.7, 0.26
	Angle		+4.76°

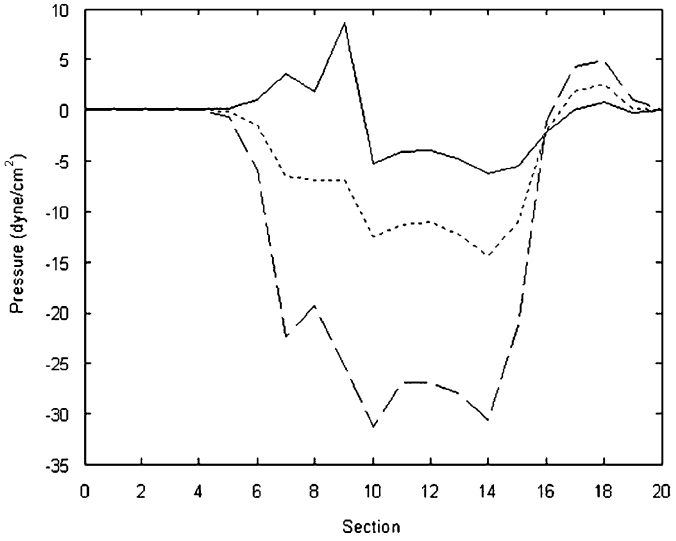

Fig. 9. Difference between the pressure distribution of larynxes with parallel glottis and widest (——), medium (·····) and narrowest (––) false vocal fold gaps, and the pressure distribution of a larynx with a parallel glottis and without false vocal folds. Minimal glottal diameter = 0.050 cm.

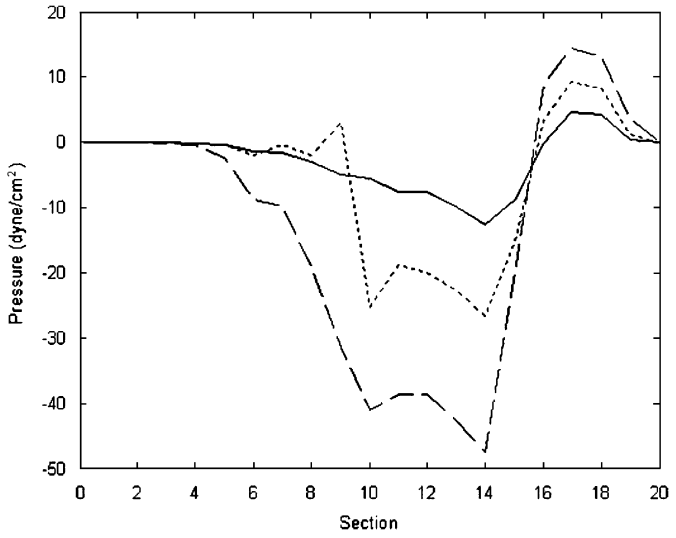

Fig. 10. Difference between the mean pressure distribution of larynxes with convergent glottis and widest (——), medium (·····) and narrowest (––) false focal fold gaps, and the mean pressure distribution of a larynx with a convergent glottis and without false vocal folds. Minimal glottal diameter = 0.050 cm.

developed upstream to this geometric point may induce this phenomenon. Further analysis should be conducted to obtain a better understanding about this.

Different false vocal fold gap sizes do affect the airflow pattern, as Fig. 11 shows. In this figure, a larynx with its glottis in divergent profile had its false vocal fold area reduced. Clearly, this reduction (pictures in the second line of Fig. 11) broke the vortex formed after the glottal constriction into two vortexes: one in the laryngeal ventricle and another beyond the false vocal folds. Also, this change in false vocal fold area keeps the jet-like shape of the airflow as a careful comparison the pictures in Fig. 11 show.

Fig. 11 also indicates the presence of vortexes near the commissure regions. Some velocity vectors located at the larynx centreline-or anterior commissure, because of the 3D visual effect-flow upstream (dark lines), independently of the size of the false vocal fold aperture.

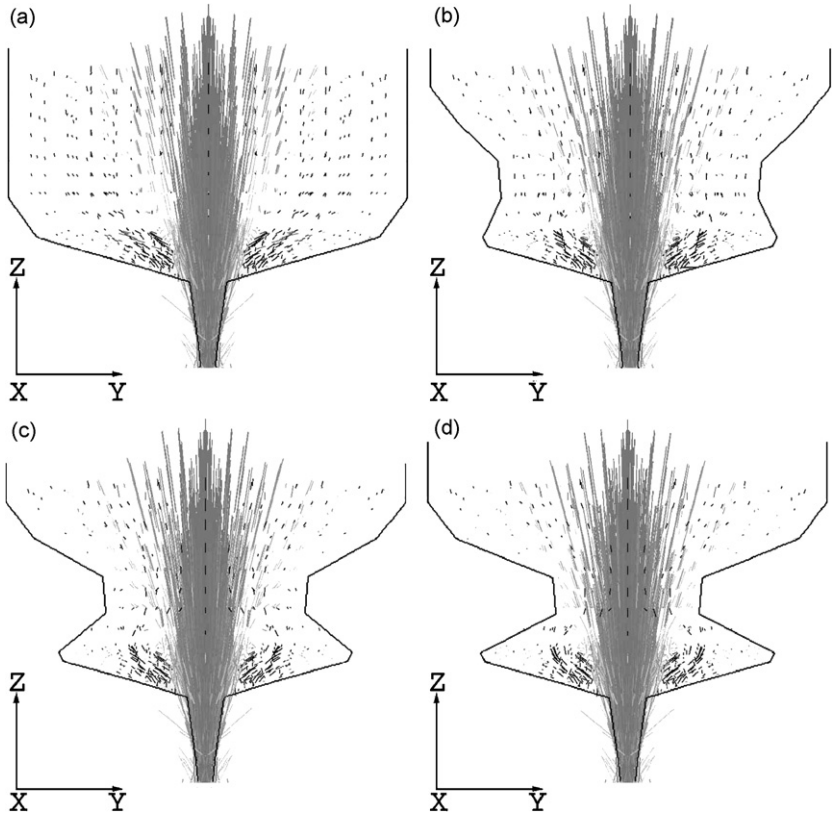

Fig. 11. 3D airflow velocity vectors in larynxes with divergent glottal profile and no (a), small (b), medium (c), and large (d) false vocal folds. Lighter vectors point downstream and darker vectors point upstream. The external boundary of the larynxes is shown.

Table 9
Airflow volume velocity for larynx with different shapes of true and false vocal folds (values in cm^3/s)

Type of FVF	Type of true vocal fold profile		
	Convergent	Divergent	Parallel
Without FVF	147.6444	204.1173	106.7644
Widest FVF gap	147.6256	204.0800	106.7602
Medium FVF gap	147.5440	203.9654	106.7429
Narrowest FVF gap	147.2334	203.5348	106.6772

Minimal glottal diameter = 0.050 cm. Transglottal pressure = 8000 dyn/cm^2.

The airflow volume velocity is also influenced by the shape of both true and false vocal folds. Table 9 shows that the divergent profile produced higher volume velocity in comparison to convergent and parallel profiles, even when the glottal sections with the minimal area among all the three profiles had the same dimensions. However, the resistance changes from no false vocal folds to narrowest false vocal folds were 0.28%, 0.29%, and 0.08% for convergent, divergent, and parallel glottis, respectively, which are negligible.

It has been demonstrated that when the ratio of the false vocal fold gap to the minimal glottal diameter is greater than 10, there is almost negligible effect on the laryngeal flow resistance [22]. As shown here, the modelled larynxes have ratios equal to $0.5/0.05 = 10$, $0.7/0.05 = 14$ and $0.9/0.05 = 18$ for the three different studied false vocal fold gaps. They produced pressure differences whose the largest value is about 30 dyn/cm^2, which is $30/8000 = 0.375\%$ of the lung pressure.

4.5. Other aspects

Because the pressure distribution curves used the mean pressure calculated for each elliptical section, and Guo and Scherer [2] gathered their curves directly from laryngeal mucosal wall surfaces, [21] shows the pressure distribution curve whose values are collected from the simulated larynx surfaces. Clearly, Guo and Scherer's results are smoother than the ones shown in Ref. [21], and in Figs. 3 and 7 because their vocal fold mesh is denser than the larynx mesh presented in Ref. [21] and here. Increasing the number of nodes and finite elements along the simulated larynx would improve the accuracy and smoothness [8] of the curves in Figs. 3, 7, 9, and 10, at the expense of computational resources. One significant difference between both works is their geometric description. Guo and Scherer's larynx channel is different at the glottal entrance and exit. Consequently, it leads the airflow separation points of both models to be different (the separation point of the present work was not calculated, because denser meshes near the glottal exit are required to obtain a reliable estimation). Additionally, their pressure magnitudes are higher due to the two-dimensionality of their models. Guo and Scherer [2] implicitly assumed a uniform longitudinal section in their 2D model. The glottal commissures of the present study, however, funnel the airflow, as presented in Fig. 11, which influences the pressure distribution pattern across the laryngeal channel. Despite these differences, both models present similar results for all the investigated laryngeal profiles: the negative pressure appears just after the channel section with the minimal area and the divergent profile produces the lowest negative pressure.

5. Conclusion

A 3D model of the larynx is presented as a method to investigate the aerodynamic behaviour relevant to phonation. The results confirm that the laryngeal section with the minimal area is responsible for defining a region of negative pressure downstream. Also, different glottal geometric profiles define different pressure distributions over the vocal fold medial surface and influence the glottal duct pressure drop. Small glottis induces high pressure gradients on the true vocal fold surfaces. The geometry of the glottal entrance also influences the airflow velocity and pressures. The smoothness of glottal entrances affects the location of the minimal pressure inside the glottis for divergent and parallel profiles ([17] in comparison with the results presented here). Considering that the current model incorporates the false vocal folds, the results presented here and [22] show that these structures negligibly affect the airflow, although a reduction in this channel area increases the glottal duct pressure drop slightly. Additionally, because the pressure distribution inside a section is nonlinear, different parts of the vocal folds are excited by different forces and, therefore, a horizontal phase difference may be characterised. The shape of the glottal commissures and the finite nature (in the longitudinal direction) of the proposed laryngeal model produce this nonlinear pressure distribution.

Mathematically, the present solution to Navier–Stokes equation seems to be very complex. However, all the algorithms and equations are well established in the literature. They were used in order to control the spurious "wiggles" that occur in the solution space for high Reynolds and gradient velocity flows, giving robustness to the final algorithm. Several aspects should be further investigated in order to verify their influence in the airflow, namely, the angle of inferior surface of the vocal folds, the angle of the false vocal fold profile, the false vocal fold gap, and the true vocal fold length. The nonlinear aspect of the airflow (represented by Navier–Stokes equations) demands several studies in order to improve the simplified models for voice synthesis. Therefore, it is believed that the proposed 3D model is another way to provide information to construct realistic synthesisers. Moreover, it is a tool that physicians can use to investigate how pressure patterns are developed over the surface of vocal folds.

Acknowledgements

The authors would like to thank the reviewers for their comments and suggestions. This work was supported by The State of São Paulo Research Foundation, Brazil (FAPESP).

References

[1] I. Titze, Phonation threshold pressure: a missing link in glottal aerodynamics, *Journal of the Acoustical Society of America* 91 (1992) 2926–2935.

[2] C. Guo, R. Scherer, Finite element simulation of glottal flow and pressure, *Journal of the Acoustical Society of America* 94 (1993) 688–700.

[3] C. Hirsh, *Numerical Computation of Internal and External Flows*, Vol. 1, Wiley, Chichester, 1988.

[4] K. Ishizaka, J. Flanagan, Synthesis of voiced sounds from a two-mass model of the vocal cords, *Bell System Technical Journal* 51 (1972) 1233–1268.

[5] J. Miller, J. Pereira, D. Thomas, Fluid flow through the larynx channel, *Journal of Sound and Vibration* 121/2 (1988) 277–290.

[6] X. Pelorson, A. Hirschberg, R. Hassel, A. Wijnands, Y. Auregan, Theoretical and experimental study of quasisteady-flow separation within the glottis during phonation, *Journal of the Acoustical Society of America* 96 (1994) 3416–3431.

[7] K. Ishizaka, Air resistance and intraglottal pressure in a model of larynx, in: I. Titze, R. Scherer (Eds.), *Vocal Fold Physiology: Biomechanics, Acoustics and Phonatory Control*, The Denver Center for Performing Arts, Denver, 1983, pp. 414–424.

[8] K.-J. Bathe, *Finite Element Procedures*, Prentice-Hall Inc., Upper Saddle River, 1996.

[9] R. Sani, P. Gresho, R. Lee, D. Griffiths, The cause and cure (?) of the spurious pressures generated by certain FEM solutions of the incompressible Navier–Stokes equations, *International Journal for Numerical Methods in Fluids* 1 (1981) 17–43.

[10] R. Sani, P. Gresho, Résumé and remarks on the open boundary condition minisymposium, *International Journal for Numerical Methods in Fluids* 18 (1994) 983–1008.

[11] *FIDAP 8 Theory Manual*, FLUENT Inc., Lebanon, NH, USA, 1998. 〈http://portal.acm.org/citation.cfm?id=937376〉.

[12] M. Tabata, S. Fujima, An upwind finite element scheme for high-Reynolds-number flows, *International Journal for Numerical Methods in Fluids* 12 (1991) 305–322.

[13] P. Sampaio, A Petrov–Galerkin formulation for the incompressible Navier–Stokes equations using equal order interpolation for velocity and pressure, *International Journal for Numerical Methods in Engineering* 31 (1991) 1135–1149.

[14] J. Peterson, The reduced basis method for incompressible viscous flow calculations, *SIAM Journal of Scientific Statistic and Computing* 10 (1989) 777–786.

[15] R. Scherer, F. Alipour, Pressure and velocity profiles in a static mechanical hemilarynx model, *Journal of the Acoustical Society of America* 112 (2002) 2996–3003.

[16] R. Scherer, D. Shinwari, K. De Witt, C. Zhang, B. Kucinschi, A. Afjeh, Intraglottal pressure profiles for a symmetric and oblique glottis with a uniform duct, *Journal of the Acoustical Society of America* 112 (2002) 1253–1256.

[17] D. Shinwari, R. Scherer, K. De Witt, A. Afjeh, Flow visualization and pressure distributions in a model of the glottis with a symmetric and oblique divergent angle of 10°, *Journal of the Acoustical Society of America* 113 (2003) 487–497.

[18] R. Scherer, D. Shinwari, K. De Witt, C. Zhang, B. Kucinschi, A. Afjeh, Intraglottal pressure profiles for a symmetric and oblique glottis with a divergence angle of 10°, *Journal of the Acoustical Society of America* 109 (2001) 1616–1630.

[19] R. Scherer, K. De Witt, B. Kucinschi, The effect of exit radii on intraglottal pressure distributions in the convergent profiles, *Journal of the Acoustical Society of America* 110 (2001) 2267–2269.

[20] M. Agarwal, R. Scherer, H. Hollien, The false vocal folds: shape and size in frontal view during phonation based on laminagraphic tracings, *Journal of Voice* 17/2 (2003) 97–113.

[21] M. Rosa, J. Pereira, M. Grellet, A. Alwan, A contribution to simulating a three-dimensional larynx model using the finite element method, *Journal of the Acoustical Society of America* 114 (2003) 2893–2905.

[22] M. Agarwal, The False Vocal Folds and Their Effects on Translaryngeal Airflow Resistance, MSc Dissertation, Bowling Green State University, 2004.